Metal-insulator transitions in epitaxial rocksalt-structure $Cr_{1-x/2}N_{1-x}O_x(001)$

Mary E. McGahay[1], Sanjay V. Khare[2], and Daniel Gall[1]
[1]*Department of Materials Science and Engineering, Rensselaer Polytechnic Institute, Troy, NY 12180, USA*
[2]*Department of Physics and Astronomy, The University of Toledo, Toledo, Ohio 43606, USA*

Substitutional replacement of N with O in epitaxial CrN(001) layers is achieved by reactive sputter deposition in a mixed N_2 and Ar + O_2 atmosphere. O incorporation facilitates Cr vacancies, yielding a rocksalt-structure solid solution $Cr_{1-x/2}N_{1-x}O_x$ with a single compositional parameter x and a measured lattice constant that decreases from a = 0.4175 to 0.4116 nm for x = 0 to 0.59. First-principles calculations predict da/dx = +0.0200, -0.0018, and -0.0087 nm for $CrN_{1-x}O_x$, $Cr_{1-x/3}N_{1-x}O_x$, and $Cr_{1-x/2}N_{1-x}O_x$, respectively, and confirm, in combination with ion beam compositional analyses and x-ray diffraction results, a vacancy concentration of $x/2$ per cation site. The room temperature resistivity decreases by over two orders of magnitudes from $\rho = 1.5\times10^{-3}$ to 7.7×10^{-6} Ω m for x = 0-0.26. This is accompanied by a transition from a negative to a positive temperature coefficient of resistivity, an increase in the Hall mobility from μ_H = 0.37 to 1.7 cm^2/Vs, an increase in the carrier concentration $n = 1.1\times10^{20}$ to 4.9×10^{21} cm^{-3}, and a decrease in the calculated bandgap from 0.54 to 0 eV. However, ρ increases again to 6.9×10^{-5} Ω m for x = 0.34 and to > 10 Ω m for $x \geq 0.59$, with a corresponding drop in μ_H and the opening of a gap. The maximum in the measured carrier density and conductivity at x = 0.26 is attributed to a maximum in the density of states near the Fermi level, in perfect agreement with calculations using supercells with randomly distributed O substitutions and Cr vacancies that predict a maximum at x = 0.25±0.05. The measurements indicate insulator-to-metal and subsequent metal-to-insulator transitions at $x = 0.04 \pm 0.03$ and 0.30 ± 0.03, respectively. The transition to metallic conduction is attributed to substitutional O on anion sites acting as donors, while the measured n for x = 0.01-0.26 quantitatively indicates charge compensation by cation vacancies that act as acceptors. The insulating properties at large x are likely caused by increased electron correlation effects.

I. Introduction

Chromium nitride has gained considerable interest because of its magnetic ordering and possible bandgap [1–4] that make it a promising material for dilute magnetic semiconductors, especially when combined with other nitride semiconductors [5–7]. Additionally, it is widely used as an oxidation and wear resistant layer in protective [8–10] and self-lubricious [11–13] hard coatings. CrN also shows promising thermoelectric properties [14–16] which are enhanced through doping with Sc [16,17], Al [18], and V [19]. Alloying CrN with CrO to form $CrN_{1-x}O_x$ has gained some interest due to its high oxidation resistance [20–22] and as a hard coating material [23,24] that combines the hardness of Cr_2O_3 with the toughness of CrN. Oxygen in rocksalt-structure $CrN_{1-x}O_x$ has a maximum solubility of x = 0.46-0.70 [20,24,25], while higher oxygen content yields corundum Cr_2O_3 [20,25–28]. Rocksalt CrO is not stable due to electron occupation of antibonding orbitals [26], but may be stabilized through vacancies [29,30]. It has been deposited on MgO(001) as an epitaxial layer through pulsed laser deposition [31]. However, most reports on CrO thin films are on layers that are just a few monolayers thick [29,32–34], as a larger thickness facilitates transformation to Cr_2O_3, the most stable chromium oxide [26].

Our recent work on the controlled oxygen exposure of CrN(001) surfaces demonstrates the formation of a conductive n-type surface oxide [35], suggesting that O may be used to form metallic Cr-N-O. These results are consistent with reports which indicate that small concentrations of oxygen impurities in CrN may increase its conductivity [36,37] while larger concentrations lead to insulating films with resistivities that are several orders of magnitude above those of stoichiometric CrN films [26,28,37,38], and also exhibit an increasing optical band gap [27,39].

In this paper, we report on the growth and electronic properties of epitaxial cubic $Cr_{1-x/2}N_{1-x}O_x$(001) layers deposited on MgO(001) by reactive sputtering using N_2 and a 90% Ar-10% O_2 gas mixture. X-ray diffraction θ-2θ scans and ω rocking-curves indicate that the layers are epitaxial and exhibit a single-phase solid-solution rocksalt structure without any detected secondary phases or

misoriented grains for $x \leq 0.59$. Temperature-dependent electronic transport measurements show a drop in the room temperature resistivity with increasing x that is attributed to an insulator-to-metal transition between $x = 0.01$ and 0.08. This trend is reversed between $x = 0.26$ and 0.34, indicating a second transition back to insulating compounds for $x \geq 0.34$. Hall measurements confirm these results which demonstrate that oxygen in CrN causes both, n-type doping and carrier localization at low and high concentrations, respectively.

II. Procedure

$Cr_{1-x/2}N_{1-x}O_x(001)$ layers were deposited in a three-chamber ultrahigh vacuum DC magnetron sputtering system with a base pressure of 10^{-9} Torr. Single-side polished 10×10×0.5 mm^3 MgO(001) wafers were cleaned with successive rinses in ultrasonic baths of tri-chloroethylene, acetone, isopropyl alcohol, and de-ionized water, inserted into the deposition system and thermally degassed in vacuum at 1000 °C for one hour. Subsequently, the substrate temperature was lowered to the deposition temperature of 750 °C. A 5-cm-diameter 99.95% pure Cr target at a distance of 10.5 cm from the substrate and at an angle of 45° was sputter cleaned with closed shutters prior to deposition. A constant flux of 99.999% pure N_2 that was further purified with a MicroTorr purifier was leaked into the chamber to reach a pressure of 10 mTorr. To achieve different compositions, a 90% Ar- 10% O_2 mixture was additionally leaked into the chamber with partial pressure p_{Ar+O2} ranging from 0-3 mTorr, yielding an oxygen partial pressure p_{O2} = 0-0.3 mTorr and a total processing gas pressure of 10-13 mTorr. A constant power of 350 W was applied to the magnetron for 45 min, yielding a growth rate of 15-27 nm/min and a resulting layer thickness of 680-1200 nm, as measured by cross-sectional scanning electron microscopy (SEM) in a FEI Versa 3D field emission scanning electron microscope using a 20 keV primary electron beam. The thickness from the micrographs was determined by contrast analysis using the software IMAGEJ.

The composition of the $Cr_{1-x/2}N_{1-x}O_x$(001) layers was determined by Rutherford (Elastic) Backscattering Spectroscopy (RBS/EBS) using 2 and 3.05 MeV $^4He^+$ ions incident at an angle of 6° relative to the sample surface normal and a total scattering angle of 166.2° between incident beam and detector. The latter energy is high enough such that Rutherford's approximation of a point charge is no longer correct and there is a resonance in the O scattering cross-section which increases the measurement's sensitivity for O. The acquired spectra were analyzed using the SIMNRA software.

X-ray diffraction (XRD) θ-2θ scans and ω-rocking curves were obtained with a PANanalytical X'Pert Pro diffractometer with a Cu Kα source. Symmetric θ-2θ scans were collected over a 2θ range of 20-90° using a parallel-beam configuration with an x-ray mirror and a PixCEL solid-state line detector operated in receiving mode with an active length of 0.165 mm. ω-rocking curves were obtained using the same source and the solid-state detector set at a constant 2θ angle corresponding to the $Cr_{1-x/2}N_{1-x}O_x$ 002 reflection, similar to what we have reported in Ref. [40].

Electron transport measurements were performed in vacuum in a Cryomagnetics Inc ^4He cryostat with a variable temperature T = 5-295 K and a superconducting magnet with a maximum 4.45 T field. 0.5-mm-wide Au-Pd contacts were sputter deposited in a Van der Pauw arrangement at the corners of 5×5 mm^2 samples. Electric contacts were completed by attaching copper wires to each of the sputter deposited contacts using indium droplets. Continuous resistivity measurements were performed during sample warm-up with 0.5 K/min from 5 to 295 K. A Keithley 2400 source meter was used as both a voltmeter and a current source, with the current adjusted depending on the sample resistance to I = 0.001, 1, or 10 mA. Hall effect measurements at 295 K were performed in the same equipment. The Hall resistance was determined from a linear fit of the measured Hall voltage as a function of the current of -40 to +40 A in the superconducting coil, yielding a continuously varying magnetic field from -4.14 to 4.14 T.

First-principles calculations were performed using the Vienna *ab initio* simulation package (VASP), employing periodic boundary conditions, a plane wave basis set, the Perdew-Burke-Ernzerhof

generalized gradient approximation exchange correlation functional [41], and the projector-augmented wave method [42]. A 550 eV cut-off energy for the plane-wave basis set and a 6×6×6 Γ-centered *k*-point grid for 64-atom supercells yield energy convergence of < 1 meV/atom. Cr 3*s*, 3*p*, 3*d*, and 4*s* electrons are explicitly calculated using the Cr_sv pseudo potential provided with the VASP package. All calculations are done using a Hubbard Coulomb term U = 3 eV which has previously been successfully applied [2,3] to describe the low-temperature antiferromagnetic CrN ground state that exhibits a 1.7° distortion from cubic symmetry [43]. Here we choose the same lowest-energy antiferromagnetic ordering with pairs of ferromagnetic Cr planes that are stacked along the [110] direction which is typically referred to as AFM $[011]_2$, but keep the structure cubic, consistent with the experimental room-temperature observation. More specifically, rocksalt structure supercells with 64 atomic sites are formed by randomly populating anion sites with N and O atoms to achieve a desired composition x. In addition, cation vacancies are introduced by removing Cr atoms at random sites but with the constraint to keep the overall magnetization minimal (i.e. antiferromagnetic) by removing the same number (or ±1) of Cr atoms with up and down magnetic moments. Each such supercell is relaxed by iteratively relaxing the atomic positions and relaxing the lattice constant a by adjusting the length of the three unit-cell vectors while keeping their length equal to each other and the angles between them at 90°. The simulated compositions include n_O = 0, 6, 12, or 18 oxygen atoms and $n_V = 0$, $n_O/3$, or $n_O/2$ Cr vacancies, yielding the compounds $CrN_{1-x}O_x$, $Cr_{1-x/3}N_{1-x}O_x$, and $Cr_{1-x/2}N_{1-x}O_x$ with x = 0, 0.1875, 0.375, and 0.5625. For each combination of n_O and n_V, three supercells with different atomic arrangements are individually relaxed, corresponding to a total of 28 simulations. The lattice constant is determined from the average of the three supercells. This approach was chosen instead of the Special Quasirandom Structures approach [44], because the variation in a from the three simulations provides an indication of the uncertainty in the determined lattice constant associated with the distribution of N and O atoms on anion sites and Cr atoms or vacancies on cation sites. We note that the random distribution of Cr vacancies also affects the arrangement of local magnetic moments such that the sampling from three independent simulations provides an indication of possible effects of the magnetic exchange on the average bond length. Such exchange striction effects have been

reported to be important for CrN [45]. The same calculations were also used to determine the total density of states DOS. However, only supercells with an even number of Cr atoms were considered in order to minimize net magnetization. Correspondingly, to achieve sufficient composition resolution, additional calculations were performed for $Cr_{1-x/2}N_{1-x}O_x$ with x = 0.125, 0.25, and 0.5, and for $CrN_{1-x}O_x$ with x = 0.03125 and 0.0625.

III. Results and Discussion

Figure 1 is a plot of the measured atomic fractions of Cr, N, and O in the deposited layers as a function of the O_2 partial pressure p_{O2}, as determined from RBS/EBS analyses. In the absence of oxygen (p_{O2} = 0), the measured Cr and N content of 49±3% and 51±3% indicate stoichiometric CrN. In contrast, increasing p_{O2} to 0.3 mTorr leads to an approximately linear increase in the oxygen content from 0 to 45±3% and a simultaneous decrease in both the N and the Cr content. This results in a decreasing cation-to-anion ratio y = [Cr]/([O]+[N]), suggesting an increasing concentration of Cr vacancies. The layer composition can in general be described as $Cr_yN_{1-x}O_x$. However, because of the approximately linear composition relationships, we can plot the measured y vs x (not shown) and use a linear function $y = a - bx$ for data fitting and find a = 0.97 and b = 0.51. These values are close to 1.0 and 0.5 so that the cation-to-anion ratio can be approximated as $y = 1 - x/2$ and throughout this paper we refer to our layers as $Cr_{1-x/2}N_{1-x}O_x$. Thus, our compositional analysis indicates that the substitutional replacement of two N by two O atoms results in the formation of one Cr vacancy. The presence of cation vacancies has previously been reported for both rocksalt CrO [25,29,32] and CrON [20,26] films and is attributed to the destabilizing effects of a high valence electron concentration [46,47], that is, cation vacancies reduce the occupation of antibonding *d*-orbitals and stabilize the rocksalt structure [26], similar to what has been reported for other column 6 nitrides like MoN [49] and WN [48,50] as well as monoxides including TiO and VO [51–53]. We note that the RBS/EBS analyses also provide quantitative information on the area

atomic density which, together with thickness measurements by SEM, show that the occupation of anion sites by nitrogen plus oxygen atoms is 1.00±0.02 for all samples, indicating a negligible vacancy concentration on anion sites.

Figure 2(a) shows sections of x-ray diffraction θ-2θ patterns from seven $Cr_{1-x/2}N_{1-x}O_x$ layers grown with different p_{O2} = 0-0.3 mTorr, as labeled. The measured intensities are plotted on a logarithmic scale and patterns from the different samples are shifted by an order of magnitude for clarity purposes. For all samples, the only peaks that can be detected in the measured 2θ range from 20-90° are within the plotted 2θ = 42-45°, indicating an 001 orientation for all layers. The double peak feature at 42.91° and 43.02° is evident in all patterns and is from the substrate MgO 002 reflections of the $Cu_{K\alpha1}$ and $Cu_{K\alpha2}$ x-rays with wavelengths of 0.15406 and 0.15444 nm, respectively. The pattern from the pure CrN layer (x = 0) exhibits in addition a similar but 7 times less intense double peak at 2θ = 43.31° and 43.43° which is from the CrN 002 reflections and indicates a CrN lattice constant a = 0.4175 nm. This is in excellent agreement with previously published values of 0.4176 and 0.4179 nm from epitaxial CrN(001) deposited by reactive sputtering on MgO(001) [1,54]. We note that all these values represent the lattice constant in the growth direction and may therefore be slightly larger than the true relaxed lattice constant because a possible compressive strain caused by differential thermal contraction during cooling from the deposition temperature that can lead to an expanded out-of-plane lattice constant. In fact, we have recently used x-ray diffraction reciprocal space maps [55] to measure a -0.31% in-plane compressive strain in a 300-nm-thick CrN(001) layer with an out-of-plane a = 0.4186 nm but a relaxed lattice constant of 0.4175 nm. This latter value perfectly matches our current measured a, suggesting that the CrN layer in this report has a negligible strain which may be attributed to the more than two-times larger thickness, facilitating relaxation through misfit dislocations. The patterns in Fig. 2 show that increasing p_{O2} causes the $Cr_{1-x/2}N_{1-x}O_x$ 002 reflections to shift to larger 2θ values, corresponding to a decreasing lattice constant with increasing oxygen content, as discussed below. In addition, peaks for alloys with p_{O2} = 0.01-0.1 mTorr are 3-5 times less intense than for pure CrN and 70 times smaller for p_{O2} = 0.2 mTorr, indicating a

decreasing crystalline quality. This suggests that the oxygen substitution degrades the crystalline quality, as also indicated by the rocking curve results discussed below. The decreasing crystalline quality is also reflected by the fact that the double peak feature can no longer be resolved for the layer with $x = 0.59$ deposited with $p_{O2} = 0.2$ mTorr. The θ-2θ scan for $p_{O2} = 0.3$ mTorr exhibits no detectable peaks from the alloy film with $x = 0.75$ over the entire measured $2\theta = 20\text{-}90°$ range, indicating a continued decrease in crystalline quality and suggesting a transition to an amorphous or nano-crystalline corundum structure that cannot be detected by our XRD measurements, consistent with the reported limit of $x = 0.46 – 0.75$ for the rocksalt-phase $CrN_{1-x}O_x$ solid solution [20,24,25]. We note that the pattern for $p_{O2} = 0.1$ mTorr exhibits a shoulder to the right of the layer peak with $2\theta = 43.9°$ that also matches the peak position for $p_{O2} = 0.2$ mTorr. We do not interpret this as the emergence of an oxide phase at large x, because (i) the peak position is inconsistent with both possible Cr_2O_3 and CrO_2 phases, (ii) the rocking curve width remains narrow (< 1°), as discussed below, and (iii) no other reflections can be detected over the entire measured 2θ range from 20-90°. Correspondingly, we attribute the shoulder and peak at $p_{O2} = 0.1$ and 0.2 mTorr to a rocksalt-structure oxynitride with some possible ordering that may lead to a slight suppression of the lattice constant.

XRD ω-rocking curves (shown as Supplemental Material [56]) from the 002 reflection of the $Cr_{1-x/2}N_{1-x}O_x$ layers are obtained using a constant 2θ value for each sample corresponding to its $K\alpha_1$ peak position. The full-width at half-maximum is 0.14° for pure CrN, indicating strong crystalline alignment of the (001) planes with the substrate surface. The width of the rocking curve increases with the addition of O to 0.26°, 0.34°, 0.32°, 0.50°, and 0.89° for $x = 0.02$, 0.08, 0.26, 0.32, and 0.59, respectively, indicating good alignment for all layers with $x \leq 0.59$ but a decreasing crystalline quality with increasing x. This confirms that the oxygen substitution degrades the crystalline quality, consistent with the decreasing peak intensity shown in Fig. 2. We note that the rocking curve of the $x = 0.59$ layer indicates a slight 0.8° tilt of the lattice planes of the layer with respect to the substrate orientation which may be caused by a strain-relaxation mechanism or may suggest a lattice distortion similar to what has been reported for the low-

temperature phase of CrN [43]. Such a 0.8° deviation from the cubic 90° results in a 0.01% reduction of the unit cell volume, which is negligible and is not considered in the below analysis.

Figure 2(b) is a plot of the lattice constant a as a function of composition x, as determined from XRD measurements on epitaxial $Cr_{1-x/2}N_{1-x}O_x(001)$ layers shown in Fig. 2(a). In addition, the plot includes calculated lattice constants from our first-principles simulations. The measured values plotted as red squares decrease from 0.4175 nm for CrN to 0.4116 nm for $Cr_{0.71}N_{0.41}O_{0.59}$. In contrast, the calculated values for $CrN_{1-x}O_x$ increase from 0.4184 nm for CrN to 0.4215, 0.4256, and 0.4302 nm for x = 0.1875, 0.375, and 0.5625. The plotted line is the result from linear curve fitting which is done by forcing the line to intercept the x = 0 data point such that the only fitting parameter is the slope da/dx = 0.0200 nm and is determined from the three $x > 0$ data points, including x = 0.5625 which is outside of the plotted a-range. The positive calculated slope indicates that substitutional replacement of N with O leads to an increasing lattice parameter. As a consequence, we attribute the negative slope from the experiment to the presence of Cr vacancies. This explanation is quantitatively explored by calculating the lattice constants of $Cr_{1-x/3}N_{1-x}O_x$ and $Cr_{1-x/2}N_{1-x}O_x$ compounds, as also shown in Fig. 2(b). The plotted error bars correspond to the standard deviation of lattice constants from multiple simulations with different anion and cation site occupations, as described in Section II. The error bars are relatively small in comparison to the absolute changes in lattice parameters, suggesting that effects from anion and cation site occupations including the related distribution of magnetic moments are negligible in comparison to compositional effects.

The calculated a for $Cr_{1-x/3}N_{1-x}O_x$ decreases very slightly, with da/dx = - 0.0018 nm. In contrast, the predicted slope for $Cr_{1-x/2}N_{1-x}O_x$ of da/dx = - 0.0087 nm is much more substantial. This is attributed to the 50% higher Cr vacancy concentration for $Cr_{1-x/2}N_{1-x}O_x$ than for $Cr_{1-x/3}N_{1-x}O_x$. The experimental lattice constants are best described by the $Cr_{1-x/2}N_{1-x}O_x$ line, confirming the compositional analyses by RBS/EBS. The negative slope is also consistent with previous studies [20,25] and has been attributed to the presence of Cr vacancies that stabilize the effects of antibonding orbital occupation with increasing x [20,26], similar to the reported increasing bond strength due to cation vacancies in transition metal monoxides

[51–53]. The lattice constant of the last datapoint at $x = 0.59$ is even slightly below the linear trend for $Cr_{1-x/2}N_{1-x}O_x$, suggesting a possible bond-length reduction associated with an ordered cubic oxynitride phase, as discussed above.

We note that assigning charges of -3, -2, and +3 to N, O, and Cr ions suggests that charge neutrality would be achieved for a composition of $Cr_{1-x/3}N_{1-x}O_x$, with an extrapolated ($x = 1$) oxide of Cr_2O_3. In contrast, the experimental measured composition of $Cr_{1-x/2}N_{1-x}O_x$ with an extrapolated CrO_2 suggests a charge of +4 for the Cr-ions in the oxide. Conversely, charge neutrality in the $Cr_{1-x/2}N_{1-x}O_x$ compound is achieved if Cr retains the nominal +3 charge and vacant cation sites have a +1 charge. In that case, the Cr-vacancies have a -2 charge relative to the +3 charge of the cations. However, the transport results presented in the following do not confirm charge neutrality but instead indicate n-type charge carriers, suggesting partial charge compensation and an approximate -1 charge (instead of the -2 required for charge neutrality) for the Cr-vacancies. That is, Cr vacancies act as acceptors and O substitutions as donors, which results in a net *n*-type semiconductor as there are twice as many O atoms than Cr vacancies in $Cr_{1-x/2}N_{1-x}O_x$.

Figure 3(a) is a plot of the measured resistivity ρ versus temperature T for $Cr_{1-x/2}N_{1-x}O_x$ films with $x = 0$-0.34. The CrN ($x = 0$) layer has a room temperature $\rho = 1.5\times10^{-3}$ Ω m, which is within the previously reported range 8.2×10^{-5} - 1.7×10^{-3} Ω m for epitaxial CrN films [1,2,5,54,57–60]. The resistivity increases with decreasing T by over two orders of magnitude to 0.37 Ω m at 5 K. This negative temperature coefficient of resistivity (TCR) is consistent with previous studies on CrN [1,5,54,57,61] and is attributed to electron transport by variable range hopping [1,59]. We note that our CrN does not exhibit a discontinuity at the 280 K phase transition temperature, which we attribute to epitaxial constraints as we have previously reported [57]. The layer with $x = 0.01$ has a resistivity of 1.0×10^{-3} and 6.9×10^{-3} Ω m at 295 and 5 K, respectively. These values are 1.5 and 54 times smaller than for CrN, indicating an increase in the conductivity and a reduction in the negative TCR with the addition of oxygen. This trend is continued with increasing x. More specifically, $x = 0.08$ and 0.26 results in metallic conduction with a

positive TCR and a room temperature $\rho = 1.4\times10^{-5}$ and 7.7×10^{-6} Ω m that is two and three orders of magnitude below that of CrN. The resistivity increases linearly with $T > 90$ K, with a measured TCR of 1.7×10^{-8} and 7.7×10^{-9} Ω m K^{-1} for $x = 0.08$ and 0.26, respectively, as determined from the slope of a linear fit between 100 and 295 K.

Increasing the O content further to $x = 0.34$ leads to an increase in the resistivity by over an order of magnitude, to 6.9×10^{-5} Ω m at 295 K and 1.1×10^{-4} Ω m at 5 K. Thus, this sample exhibits a negative TCR, indicating a transition back towards insulating compositions. The resistivity of samples with $x = 0.59$ and 0.75 are too high to be measured with our experimental setup. Thus, they are much more resistive, with an estimated lower bound for the resistivity: $\rho > 10$ Ω m for $x \geq 0.59$.

Figure 3(b) is a plot of the carrier concentration n and Hall mobility μ_H versus x, as determined from Hall effect measurements which indicate a linear dependency of the Hall voltage with applied magnetic field. The carrier concentration increases by nearly two orders of magnitude from 1.1×10^{20} cm^{-3} for $x = 0$ to 1.7×10^{20}, 1.8×10^{21} and 4.9×10^{21} cm^{-3} for $x = 0.01$, 0.08, and 0.26, respectively, followed by a slight decrease to 4.0×10^{21} cm^{-3} for $x = 0.34$. The large plotted uncertainty for the last ($x = 0.34$) sample is due to unreliable electric contacts to this oxygen-rich sample which resulted in a large thermal drift in the measured Hall voltage and also missing data points between 70 and 125 K in Fig. 3(a). The Hall mobility is 0.37 and 0.35 cm^2/Vs for $x = 0$ and 0.01, increases to $\mu_H = 2.4$ cm^2/Vs for $x = 0.08$, but then decreases again to $\mu_H = 1.7$ and 0.28 cm^2/Vs for $x = 0.26$ and 0.34.

The relatively low $\mu_H = 0.37$ cm^2/Vs for pure CrN is in reasonable agreement with previously reported [1] values of 0.16 and 0.19 cm^2/Vs and is attributed to carrier localization [1,57] caused by the Mott-Hubbard interaction which splits the filled and empty d_{t2g} bands below the valence band maximum and above the conduction band minimum, respectively, resulting in a *p*-to-*d* charge transfer band gap [2]. We note that the cause for carrier localization here is distinctly different from what has been reported for other transition metal nitrides where localization has been attributed to (1) complete charge depletion in

the *d*-bands causing a gap between hybridized *p* and *d* bands like for ScN [62], $Sc_{1-x}Al_xN$ [63], and $Ti_{1-x}Mg_xN$ [64], and (2) weak Anderson localization due to random arrangement of nitrogen vacancies in TaN_x [65,66], NbN_x [67], and HfN_x [68], or random cation site occupation in $Sc_{1-x}Ti_xN$ [69] and $Ti_{1-x}W_xN$ [70]. Our $Cr_{1-x/2}N_{1-x}O_x(001)$ layer with $x = 0.01$ has a comparable room-temperature carrier concentration and mobility as the pure CrN layer, but the resistivity at 5 K is nearly two orders of magnitude lower, suggesting a decrease in localization. Increasing the O concentration further to reach $x = 0.08$ and 0.26 results in a dramatic increase in both n and μ_H, suggesting a transition to metallic conduction in a highly degenerate semiconductor, as also evidenced by the positive TCR for $x = 0.08$ and 0.26. This is consistent with previous studies reporting increasing conduction with the substitutional replacement of N with O in CrN [36,37]. Simple electron counting suggests that substitutional O on an anion site in CrN provides an extra electron and therefore is expected to act as n-type dopant. However, our samples also contain an increasing number of Cr vacancies with increasing x. Cr vacancies have been reported to cause p-type conduction in CrN [18] and are therefore expected to counteract the n-type doping by O. For example, the $x = 0.01$ sample contains 5.5×10^{20} cm^{-3} O atoms and 2.8×10^{20} cm^{-3} Cr vacancies which are expected to act as donors and acceptors, respectively. The difference of 2.7×10^{20} cm^{-3} between the donor and acceptor density corresponds to the expected carrier concentration, which is in reasonable agreement with the measured $n = 1.7\times10^{20}$ cm^3. Similarly, $x = 0.08$ and 0.26 yield expected carrier concentrations of 2.2×10^{21} and 7.2×10^{21} cm^{-3}, in good agreement with the measured $n = 1.8\times10^{21}$ and 4.9×10^{21} cm^{-3}. Thus, the measured n in our samples with low O content ($x = 0.01$-0.26) is well explained by substitutional oxygen and Cr vacancies acting as compensating donors and acceptors, respectively. However, increasing x further to 0.34 results in a reduction in both n and μ_H, as well as an increase in ρ and a transition to a negative TCR, indicating a metal-insulator transition. This is consistent with a reported increase in resistivity with increasing O content [26,28,37,38] and is attributed to the increasing localization from O 2p orbitals and potential fluctuations due to the random anion site occupation resulting in increasing electron correlation. Samples with $x > 0.34$ become increasingly more resistive with increasing x. We note that this cannot be explained by simple extrapolation of our chemical formula $Cr_{1-x/2}N_{1-x}O_x$ to $x = 1$,

which yields CrO_2 that is half-metallic with a relatively low room-temperature resistivity of 2.5×10^{-6} Ω m [71]. In contrast, our XRD analyses for $x = 0.59$ indicate a single-phase epitaxial layer with a rocksalt-derived structure with some possible ordering on cation or anion sites, as discussed above. Thus, the data indicates a transition to insulating properties without a structural phase transition with increasing $x \leq 0.59$. Nevertheless, increasing the oxygen content further to $x = 0.75$ results in a structure without a detectable XRD peak, suggesting an amorphous or nanocrystalline corundum-like structure, consistent with previous studies on $CrN_{1-x}O_x$ films that report a transition to a Cr_2O_3 structure at large x [20,21,26–28].

Figure 4 shows the results from our density of states calculations which provide further quantitative insight into the insulator-to-metal-to-insulator transitions. The DOS in Fig. 4(a) for pure CrN shows a double peak feature associated with the hybridized N2p-Cr3d_{t2g} valence band between E = -8.0 and -0.5 eV and a bandgap of 0.54 eV. The Fermi level $E_f = 0$ eV is set to the bottom of the conduction band and the y-axis is the total DOS of the 64 atom unit cell including both spins, such that the integral of the plotted DOS for $E < E_f$ is $32\times(6+3) = 288$, corresponding to 32 N and 32 Cr atoms with 6 and 3 valence electrons, respectively. The plotted DOS as well as the band gap value are in good agreement with previous studies [2], but we note that particularly the bandgap is a strong function of the chosen U = 3 eV and is also a function of the simulated phase, which is here the cubic AFM $[011]_2$ structure as discussed in Section II. Figs. 4(b-d) show the calculated DOS for $Cr_{1-x/2}N_{1-x}O_x$ with x = 0.125, 0.25, and 0.5, respectively. The three differently colored symbols in each plot are from three simulated unit cells with different random placement of oxygen atoms on anion sites and Cr vacancies on cation sites, as described in Section II. Thus, the three colors provide a quantitative measure of the variation in the DOS associated with the random site occupation. The DOS for $x = 0.125$ in Fig. 4(b) exhibits a double peak feature from the conduction band and a drop to zero near E_f, similar to the DOS for CrN. However, the band gap is smaller, 0.16, 0.19, and 0.28 eV for the three configurations, yielding an average E_g = 0.21±0.05 eV. Increasing the oxygen content to $x = 0.25$ results in states near E_f such that the DOS remains finite for all three simulated super cells, as shown in Fig. 4(c), yielding a zero gap $E_g = 0$ eV.

However, increasing the oxygen content further to $x = 0.5$ opens again a gap of $E_g = 0.39 \pm 0.06$ eV. In summary, the plotted DOS in Figs. 4(a-d) show that the calculated bandgap of $Cr_{1-x/2}N_{1-x}O_x$ decreases with increasing $x < 0.25$, but increases again for $x > 0.25$, in direct agreement with the measured insulator-to-metal and subsequent metal-to-insulator transitions.

Figure 4(e) is a plot of the DOS near E_f vs x in $CrN_{1-x}O_x$, $Cr_{1-x/3}N_{1-x}O_x$, and $Cr_{1-x/2}N_{1-x}O_x$. The values are obtained by averaging over the calculated DOS at $E = E_f \pm 0.3$ eV where the ±0.3 eV interval was chosen sufficiently large to average over the strong DOS oscillations shown in Figs. 4(a-d) which are characteristic of specific cation and anion site occupations. The plotted error bars in Fig. 4(e) correspond to the standard deviation from three different configurations, as shown as three colors in e.g. Fig. 4(b). No error bar is given for $x = 0$, 0.03125, and 0.0625, because only one configuration was calculated for zero, one, or two oxygen atoms per super cell, each. The three data sets each show a maximum in the DOS(E_f) at an intermediate oxygen content. The data most relevant to the experimental samples is for $Cr_{1-x/2}N_{1-x}O_x$, plotted as grey diamonds in Fig. 4(e). It exhibits a maximum at $x = 0.25 \pm 0.05$. This almost perfectly matches the composition $x = 0.26$ of the sample with the highest measured $n = 4.9 \times 10^{21}$ cm^{-3} and the lowest measured resistivity. Thus, the calculated DOS(E_f) provide a semiquantitative explanation for the increase and subsequent decrease in the measured carrier concentration with increasing x in $Cr_{1-x/2}N_{1-x}O_x$.

IV. Conclusions

Epitaxial $Cr_{1-x/2}N_{1-x}O_x(001)$ layers were grown on MgO(001) substrates by reactive magnetron sputtering at 750 °C in a N_2 and Ar + O_2 atmosphere. Increasing p_{O2} from 0 to 0.3 mTorr results in films with O content x = 0-0.75 as determined by RBS and EBS. X-ray diffraction analyses indicate a rocksalt solid solution for $x \leq 0.59$ and a decreasing lattice constant $a = 0.4175$ nm for pure CrN to $a = 0.4116$ nm for $x = 0.59$. This decrease is attributed to the presence of Cr vacancies, also detected by RBS/EBS measurements, and agrees well with the predicted lattice constants from density functional theory

calculations. The decrease in the room temperature resistivity from 1.5×10^{-3} Ω m for $x = 0$ to 1.4×10^{-5} Ω m for $x = 0.08$ and the change from a negative to a positive TCR indicate an insulator-to-metal transition at $x = 0.04 \pm 0.03$. This transition is accompanied by a substantial increase in n from 1.1×10^{20} cm^{-3} for $x = 0$ to 1.8×10^{21} cm^{-3} for $x = 0.08$ and a sharp increase in μ_H from 0.37 to 2.4 cm^2/Vs. These results suggest that substituting N with O on anion sites of CrN results in n-type doping which, however, is partially compensated by Cr vacancies that have a -1 charge and act as acceptors. This interpretation is consistent with density of states calculations which show that the band gap decreases and then vanishes with increasing $x = 0.0$-0.25. Increasing the oxygen content further to $x = 0.34$ and beyond reverses the trend, resulting in an increase in ρ, a decrease in n and μ_H, a negative TCR, a decrease in the calculated DOS near E_f and the opening of a band gap. This suggests a transition to insulating properties which are attributed to carrier localization and electron correlation effects that dominate at $x = 0.34$ and become much more pronounced as x is increased to 0.59. Even higher oxygen content causes a transition to a nanocrystalline or amorphous structure at $x = 0.75$.

Acknowledgments

The authors acknowledge financial support by the National Science Foundation under Grant Nos. 1712752, 1629230, and 1629239 and by the Sandia National Laboratories. Computational resources were provided by the Center for Computational Innovations at RPI.

Figures

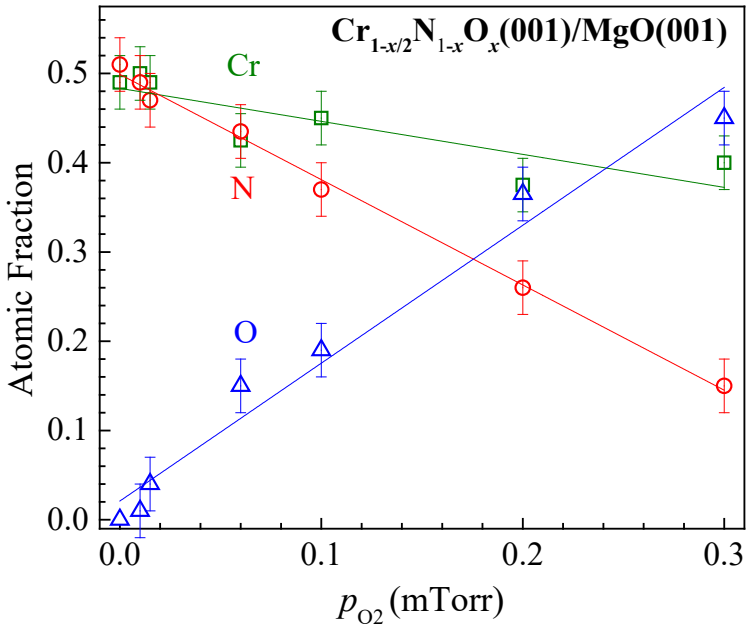

Figure 1: Layer composition measured by RBS/EBS and plotted as atomic fractions of Cr, N, and O, vs O_2 partial pressure p_{O2} during layer deposition.

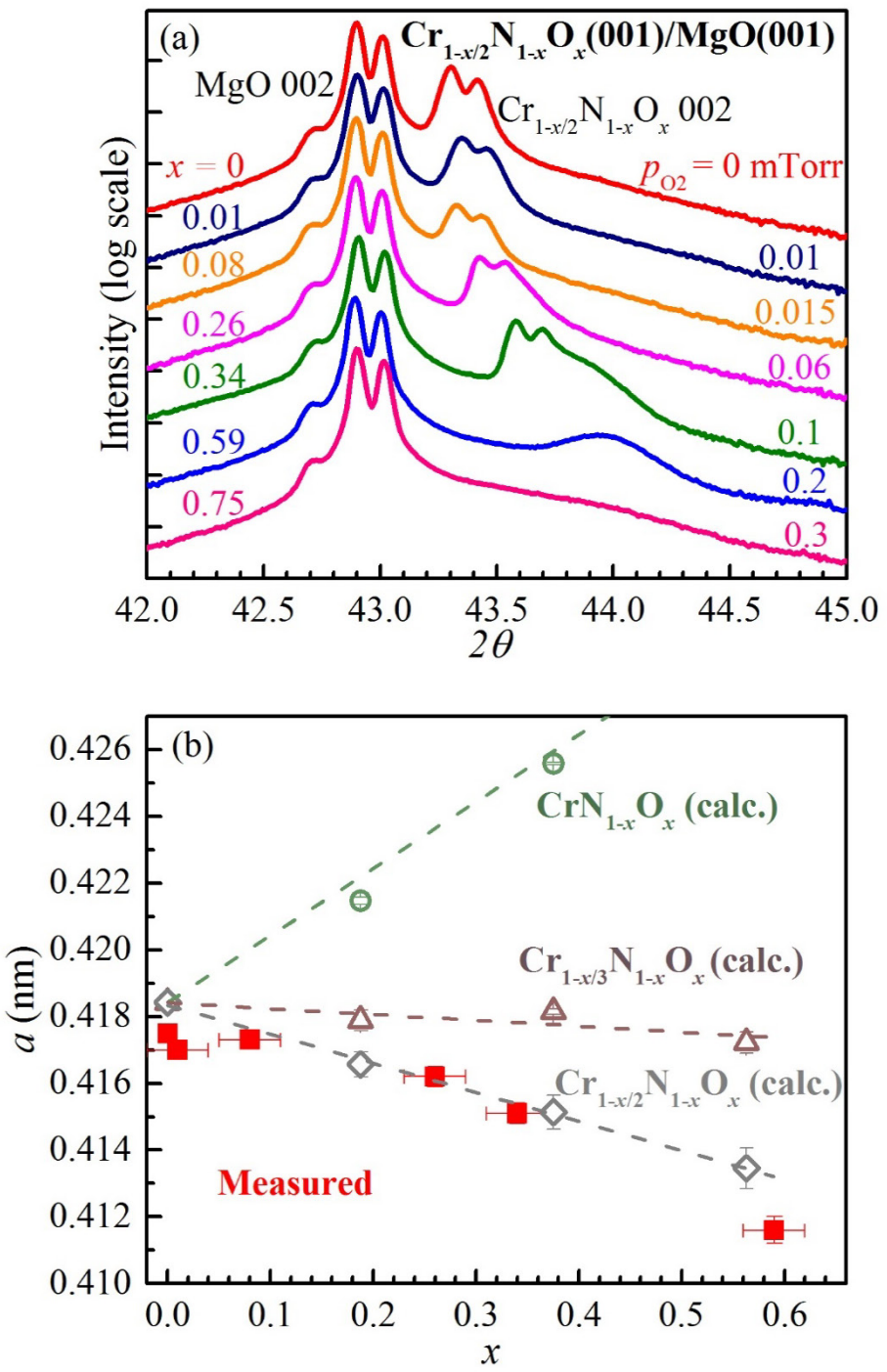

Figure 2: (a) X-ray diffraction θ-2θ scans from epitaxial $Cr_{1-x/2}N_{1-x}O_x$(001) layers grown on MgO(001) with p_{O2} = 0-0.3 mTorr. (b) Lattice constant a vs x, as measured by XRD from $Cr_{1-x/2}N_{1-x}O_x$(001) layers (red squares), and determined from first-principles calculations for $CrN_{1-x}O_x$ (green circles), $Cr_{1-x/3}N_{1-x}O_x$ (maroon triangles), and $Cr_{1-x/2}N_{1-x}O_x$ (grey diamonds).

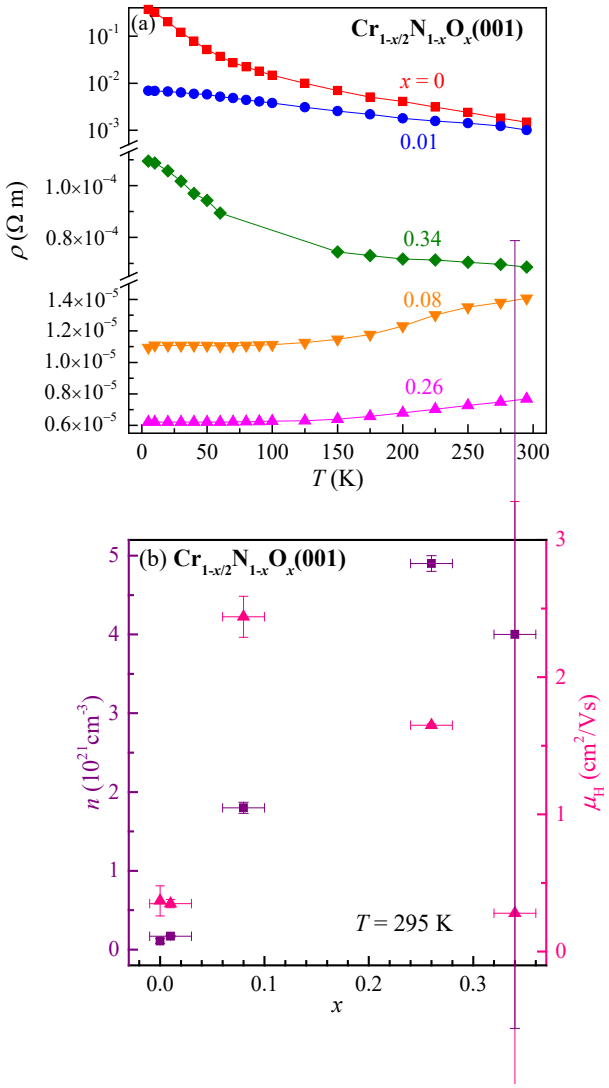

Figure 3: (a) Electrical resistivity ρ vs temperature T and (b) room-temperature carrier concentration n (purple) and Hall mobility μ_H (pink) vs x of epitaxial $Cr_{1-x/2}N_{1-x}O_x$(001)/MgO(001) layers.

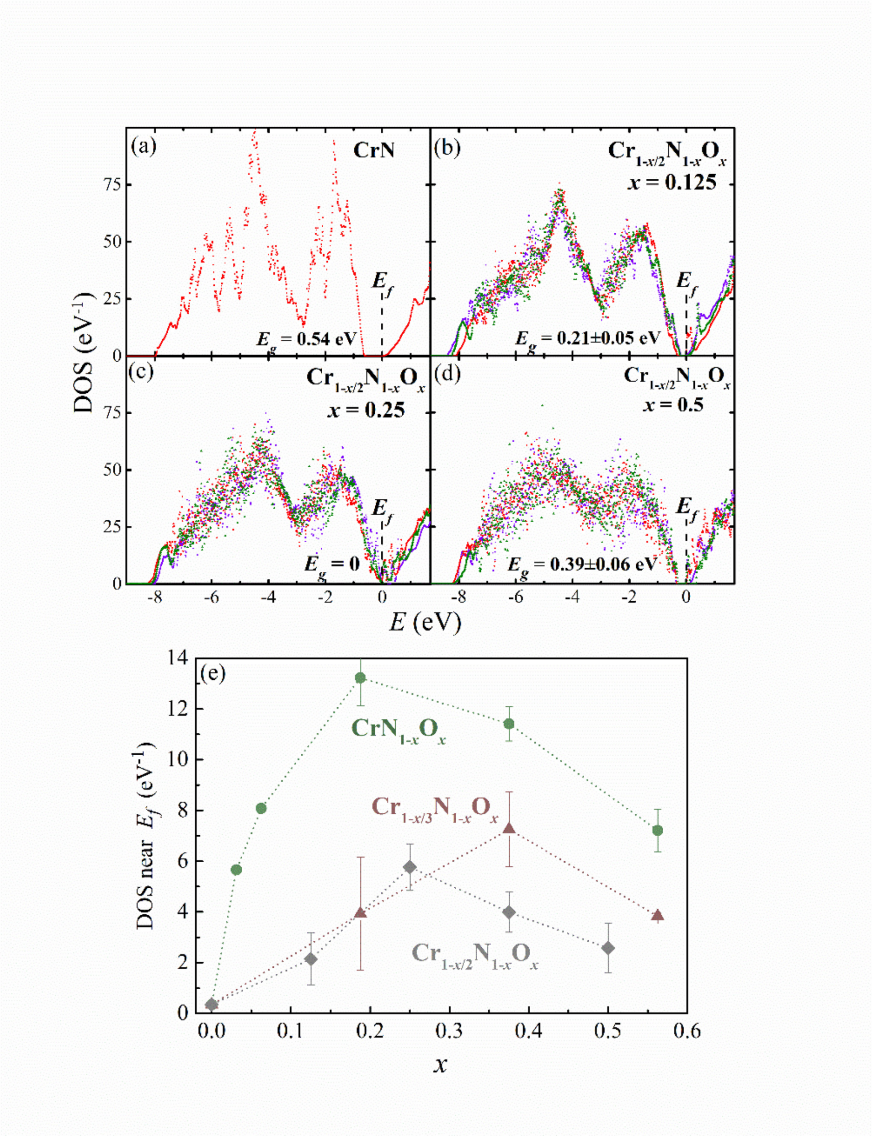

Figure 4: Calculated density of states DOS vs energy E for (a) CrN, (b-d) $Cr_{1-x/2}N_{1-x}O_x$ with x = 0.125, 0.25, and 0.5, respectively, and (e) the DOS near the Fermi level E_f vs x in $CrN_{1-x}O_x$, $Cr_{1-x/3}N_{1-x}O_x$, and $Cr_{1-x/2}N_{1-x}O_x$. The three colors in (b-d) are from three separate calculations with different random cation and anion site occupations.

References

[1] X.Y. Zhang, J.S. Chawla, B.M. Howe, and D. Gall, Phys. Rev. B **83**, 165205 (2011).

[2] A. Herwadkar and W.R.L. Lambrecht, Phys. Rev. B **79**, 035125 (2009).

[3] B. Alling, T. Marten, and I.A. Abrikosov, Phys. Rev. B **82**, 184430 (2010).

[4] I. Stockem, A. Bergman, A. Glensk, T. Hickel, F. Körmann, B. Grabowski, J. Neugebauer, and B. Alling, Phys. Rev. Lett. **121**, 125902 (2018).

[5] P.A. Anderson, R.J. Kinsey, S.M. Durbin, A. Markwitz, V.J. Kennedy, A. Asadov, W. Gao, and R.J. Reeves, J. Appl. Phys. **98**, 043903 (2005).

[6] A. Ney, R. Rajaram, S.S.P. Parkin, T. Kammermeier, and S. Dhar, Appl. Phys. Lett. **89**, 112504 (2006).

[7] A. Ney, R. Rajaram, S.S.P. Parkin, T. Kammermeier, and S. Dhar, Phys. Rev. B **76**, 035205 (2007).

[8] P. Panjan, B. Navinšek, A. Cvelbar, A. Zalar, and I. Milošev, Thin Solid Films **281**–**282**, 298 (1996).

[9] P. Hones, C. Zakri, P.E. Schmid, F. Lévy, and O.R. Shojaei, Appl. Phys. Lett. **76**, 3194 (2000).

[10] I. Milošev, J.M. Abels, H. -H. Strehblow, B. Navinšek, and M. Metikoš-Hukovič, J. Vac. Sci. Technol. A Vacuum, Surfaces, Film. **14**, 2527 (1996).

[11] C.P. Mulligan and D. Gall, Surf. Coatings Technol. **200**, 1495 (2005).

[12] C.P. Mulligan, T.A. Blanchet, and D. Gall, Surf. Coatings Technol. **203**, 584 (2008).

[13] C.P. Mulligan, T.A. Blanchet, and D. Gall, Surf. Coatings Technol. **204**, 1388 (2010).

[14] C.X. Quintela, J.P. Podkaminer, M.N. Luckyanova, T.R. Paudel, E.L. Thies, D.A. Hillsberry, D.A. Tenne, E.Y. Tsymbal, G. Chen, C.B. Eom, and F. Rivadulla, Adv. Mater. **27**, 3032 (2015).

[15] C.X. Quintela, F. Rivadulla, and J. Rivas, Appl. Phys. Lett. **94**, 152103 (2009).

[16] P. Eklund, S. Kerdsongpanya, and B. Alling, J. Mater. Chem. C **4**, 3905 (2016).

[17] S. Kerdsongpanya, B. Sun, F. Eriksson, J. Jensen, J. Lu, Y.K. Koh, N. Van Nong, B. Balke, B. Alling, and P. Eklund, J. Appl. Phys **120**, 215103 (2016).

[18] A. le Febvrier, N. Van Nong, G. Abadias, and P. Eklund, Appl. Phys. Express **11**, 051003 (2018).

[19] C.X. Quintela, B. Rodríguez-González, and F. Rivadulla, Appl. Phys. Lett. **104**, 022103 (2014).

[20] L. Castaldi, D. Kurapov, A. Reiter, V. Shklover, P. Schwaller, and J. Patscheider, Surf. Coatings Technol. **203**, 545 (2008).

[21] K. Suzuki, T. Endo, A. Sato, T. Suzuki, T. Nakayama, H. Suematsu, and K. Niihara, Mater. Trans. **54**, 1957 (2013).

[22] J. Inoue, H. Asami, M. Hirai, T. Suzuki, H. Suematsu, W. Jiang, and K. Yatsui, Trans. Inst. Electr. Eng. Japan.A **124**, 496 (2004).

[23] T. Suzuki, J. Inoue, H. Saito, M. Hirai, H. Suematsu, W. Jiang, and K. Yatsui, Thin Solid Films **515**, 2161 (2006).

[24] M. Urgen, V. Ezirmik, E. Senel, Z. Kahraman, and K. Kazmanli, Surf. Coatings Technol. **203**, 2272 (2009).

[25] K. Suzuki, T. Endo, T. Fukushima, A. Sato, T. Suzuki, T. Nakayama, H. Suematsu, and K. Niihara, Mater. Trans. **54**, 1140 (2013).

[26] L. Castaldi, D. Kurapov, A. Reiter, V. Shklover, and J. Patscheider, J. Appl. Phys. **109**, 53720 (2011).

[27] S.K. Rawal, A.K. Chawla, V. Chawla, R. Jayaganthan, and R. Chandra, Thin Solid Films **519**, 7686 (2011).

[28] R. Mientus, R. Grötschel, and K. Ellmer, Surf. Coatings Technol. **200**, 341 (2005).

[29] M. Schmid, G. Leonardelli, M. Sporn, E. Platzgummer, W. Hebenstreit, M. Pinczolits, and P. Varga, Phys. Rev. Lett. **82**, 355 (1999).

[30] A. Eichler and J. Hafner, Phys. Rev. B **62**, 5163 (2000).

[31] K. Suzuki, T. Suzuki, Y. Nakajima, Y. Matsui, H. Suematsu, T. Nakayama, and K. Niihara, APL Mater. **3**, 96105 (2015).

[32] X.S. Du, S. Hak, T. Hibma, O.C. Rogojanu, and B. Struth, J. Cryst. Growth **293**, 228 (2006).

[33] A. Maetaki and K. Kishi, Surf. Sci. **411**, 35 (1998).

[34] A. Maetaki, M. Yamamoto, H. Matsumoto, and K. Kishi, Surf. Sci. **445**, 80 (2000).

[35] M.E. McGahay and D. Gall, Appl. Phys. Lett. **114**, 131602 (2019).

[36] P. Tomeš, D. Logvinovich, J. Hejtmánek, M.H. Aguirre, and A. Weidenkaff, Acta Mater. **59**, 1134 (2011).

[37] S. Nagasawa, K. Suzuki, A. Sato, T. Suzuki, T. Nakayama, H. Suematsu, and K. Niihara, Jpn. J. Appl. Phys. **55**, 02BC18 (2016).

[38] R. Arvinte, J. Borges, R.E. Sousa, D. Munteanu, N.P. Barradas, E. Alves, F. Vaz, and L. Marques, Appl. Surf. Sci. **257**, 9120 (2011).

[39] R. Mientus and K. Ellmer, Surf. Coatings Technol. **116**–**119**, 1093 (1999).

[40] B. Wang, K. Aryana, J.T. Gaskins, P.E. Hopkins, S. V Khare, and D. Gall, Adv. Funct. Mater. 2001915 (2020).

[41] J.P. Perdew, K. Burke, and M. Ernzerhof, Phys. Rev. Lett. **77**, 3865 (1996).

[42] G. Kresse and D. Joubert, Phys. Rev. B **59**, 1758 (1999).

[43] L.M. Corliss, N. Elliott, and J.M. Hastings, Phys. Rev. **117**, 929 (1960).

[44] A. Zunger, S.H. Wei, L.G. Ferreira, and J.E. Bernard, Phys. Rev. Lett. **65**, 353 (1990).

[45] F. Rivadulla, M. Bañobre-López, C.X. Quintela, A. Piñeiro, V. Pardo, D. Baldomir, M.A. López-Quintela, J. Rivas, C.A. Ramos, H. Salva, J.-S. Zhou, and J.B. Goodenough, Nat. Mater. **8**, 947 (2009).

[46] K. Balasubramanian, S. V. Khare, and D. Gall, Acta Mater. **152**, 175 (2018).

[47] K. Balasubramanian, S. V. Khare, and D. Gall, Acta Mater. **159**, 77 (2018).

[48] K. Balasubramanian, S. Khare, and D. Gall, Phys. Rev. B **94**, 174111 (2016).

[49] B.D. Ozsdolay, K. Balasubramanian, and D. Gall, J. Alloys Compd. **705**, 631 (2017).

[50] B.D. Ozsdolay, C.P. Mulligan, K. Balasubramanian, L. Huang, S. V Khare, and D. Gall, Surf. Coatings Technol. **304**, 98 (2016).

[51] J.B. Goodenough, Phys. Rev. B **5**, 2764 (1972).

[52] M.D. Banus, T.B. Reed, and A.J. Strauss, Phys. Rev. B **5**, 2775 (1972).

[53] F. Rivadulla, J. Fernández-Rossier, M. García-Hernández, M.A. López-Quintela, J. Rivas, and J.B. Goodenough, Phys. Rev. B **76**, 205110 (2007).

[54] D. Gall, C.-S. Shin, T. Spila, M. Odén, M.J.H. Senna, J.E. Greene, and I. Petrov, J. Appl. Phys. **91**, 3589 (2002).

[55] M.E. McGahay, B. Wang, J. Shi, and D. Gall, Phys. Rev. B **101**, 205206 (2020).

[56] See Supplemental Material at http://link.aps.org/supplemental/ 10.1103/PhysRevB.xx.xxxxxx for the 002 rocking curve plots.

[57] X.Y. Zhang, J.S. Chawla, R.P. Deng, and D. Gall, Phys. Rev. B **84**, 73101 (2011).

[58] X.Y. Zhang and D. Gall, Phys. Rev. B **82**, 045116 (2010).

[59] D. Gall, C.-S. Shin, R.T. Haasch, I. Petrov, and J.E. Greene, J. Appl. Phys. **91**, 5882 (2002).

[60] K. Inumaru, K. Koyama, N. Imo-oka, and S. Yamanaka, Phys. Rev. B **75**, 054416 (2007).

[61] R. Sanjinés, O. Banakh, C. Rojas, P.E. Schmid, and F. Lévy, Thin Solid Films **420**–**421**, 312 (2002).

[62] R. Deng, B.D. Ozsdolay, P.Y. Zheng, S. V Khare, and D. Gall, Phys. Rev. B **91**, 45104 (2015).

[63] R. Deng, P.Y. Zheng, and D. Gall, J. Appl. Phys. **118**, 015706 (2015).

[64] B. Wang, S. Kerdsongpanya, M.E. McGahay, E. Milosevic, P. Patsalas, and D. Gall, J. Vac. Sci. Technol. A **36**, 061501 (2018).

[65] C.-S. Shin, D. Gall, P. Desjardins, A. Vailionis, H. Kim, I. Petrov, J.E. Greene, and M. Odén, Appl. Phys. Lett. **75**, 3808 (1999).

[66] C.-S. Shin, D. Gall, Y.-W. Kim, P. Desjardins, I. Petrov, J.E. Greene, M. Odén, and L. Hultman, J. Appl. Phys. **90**, 2879 (2001).

[67] K. Zhang, K. Balasubramanian, B.D. Ozsdolay, C.P. Mulligan, S. V. Khare, W.T. Zheng, and D. Gall, Surf. Coatings Technol. **288**, 105 (2016).

[68] H.-S. Seo, T.-Y. Lee, I. Petrov, J.E. Greene, and D. Gall, J. Appl. Phys. **97**, 083521 (2005).

[69] D. Gall, I. Petrov, and J.E. Greene, J. Appl. Phys. **89**, 401 (2001).

[70] F. Tian, J. D'Arcy-Gall, T.-Y. Lee, M. Sardela, D. Gall, I. Petrov, and J.E. Greene, J. Vac. Sci. Technol. A **21**, 140 (2003).

[71] D. S. Rodbell, J. M. Lommel, and R. C. Devries, J. Phys. Soc. Japan **21**, 2430 (1966).